Atmospheric
Measurement
Techniques

Algorithm for vertical distribution of boundary layer aerosol components in remote-sensing data

Futing Wang[1,2], **Ting Yang**[1,3], **Zifa Wang**[1,2,3], **Haibo Wang**[1,2], **Xi Chen**[1,2], **Yele Sun**[1,2], **Jianjun Li**[4], **Guigang Tang**[4], **and Wenxuan Chai**[4]

[1]State Key Laboratory of Atmospheric Boundary Layer Physics and Atmospheric Chemistry,
Institute of Atmospheric Physics, Chinese Academy of Sciences, Beijing, 100029, China
[2]College of Earth and Planetary Sciences, University of Chinese Academy of Sciences, Beijing, 100049, China
[3]Center for Excellence in Regional Atmospheric Environment, Institute of Urban Environment,
Chinese Academy of Sciences, Xiamen, 361021, China
[4]China National Environmental Monitoring Center, Beijing, China

Correspondence: Ting Yang (tingyang@mail.iap.ac.cn)

Abstract. The vertical distribution of atmospheric aerosol components is vital to the estimation of radiative forcing and the catalysis of atmospheric photochemical processes. Based on the synergy of ground-based lidar and sun-photometer in Generalized Aerosol Retrieval from Radiometer and Lidar Combined data (GARRLiC), this paper developed a new algorithm to get the vertical mass concentration profiles of fine-mode aerosol components for the first time. Retrieval of aerosol properties was achieved based on the sky radiance at multiple scatter angles, total optical depth (TOD) at 440, 675, 870, and 1020 nm, and lidar signals at 532 and 1064 nm. In addition, the internal mixing model and normalized volume size distribution (VSD) model were established according to the absorption and water solubility of the aerosol components, to separate the profiles of black carbon (BC), water-insoluble organic matter (WIOM), water-soluble organic matter (WSOM), ammonium nitrate-like (AN), and fine aerosol water (AW) content. Results showed a reasonable vertical distribution of aerosol components compared with in situ observations and reanalysis data. The estimated and observed BC concentrations matched well with a correlation coefficient up to 0.91, while there was an evident overestimation of organic matter (OM = WIOM + WSOM, NMB = 0.98). Moreover, the retrieved AN concentrations were closer to the simulated results ($R = 0.85$), especially in polluted conditions. The BC and OM correlations were relatively weaker, with a correlation coefficient of ~ 0.5. Be-

sides, the uncertainties caused by the input parameters (i.e., relative humidity (RH), volume concentration, and extinction coefficients) were assessed using the Monte Carlo method. The AN and AW had smaller uncertainties at higher RH. Herein, the proposed algorithm was also applied to remote-sensing measurements in Beijing with two typical cases. In the clean condition with low RH, there were comparable AN and WIOM, but peaking at different altitudes. On the other hand, in the polluted case, AN was dominant and the maximum mass concentration occurred near the surface. We expected that the algorithm could provide a new idea for lidar inversion and promote the development of aerosol component profiles.

1 Introduction

Atmospheric aerosols play a key role in the radiation budget and energy balance (Andrews and Forster, 2020; Hasekamp et al., 2019). The aerosols with different optical and physical properties have diverse radiative forcing effects (Boucher et al., 2013). For example, the soot dominated by black carbon (BC) has the most significant effect on cloud cover and precipitation due to its strong absorption (Gu et al., 2006; Xia, 2014), while the negative radiative forcing of sulfate and nitrate is more prominent (Myhre et al., 2013). Especially, different aerosol components can even cause opposite

radiation changes vertically (Jiang et al., 2013). On the other hand, aerosols can affect the atmospheric oxidation capacity by changing the photolysis rate of trace gases (Bian et al., 2003; Lou et al., 2014; Xing et al., 2017). Liao et al. (1999) once found that nonabsorbent aerosols generally enhanced photolysis rates, contrary to the soot aerosols. Moreover, the ability of aerosols to reduce the photolysis frequency of O_3 decreases with altitude on a regional scale (Li et al., 2011). Therefore, the vertical distribution of atmospheric aerosol components is of vital importance to reduce the uncertainty of radiative forcing estimation and understand the impact of haze on atmospheric photochemical processes.

At present, there are many studies focusing on the aerosol components on the ground (Han et al., 2015; Huang et al., 2014; Zhao et al., 2013). However, the ways to get the aerosol components in the atmosphere are finite. Although the field campaigns often launched aircraft (Chen et al., 2009; Zhang et al., 2009) or tethered balloons (Li et al., 2015; Ran et al., 2016) to detect the atmospheric structure, there are still many limitations in the resolution and representation due to the restricted aircraft control. In such a situation, continuous remote-sensing technology with high temporal resolution, such as sun-photometer and lidar, provides a powerful tool for the identification of aerosol components. Besides, the establishment of ground-based networks, e.g., AERONET (Dubovik et al., 2002, 2000), AD-Net (Shimizu et al., 2017; Nishizawa et al., 2017), and MPLNET (Chew et al., 2013; Huang et al., 2011), also improves the spatial detection resolution.

So far, the algorithms that use instantaneous remote-sensing measurements to retrieve atmospheric aerosol components have been greatly developed. The available aerosol parameters from sun-photometer make it possible to distinguish the components. Schuster et al. (2005) proposed a three-component model constrained by the refractive index to infer BC, ammonium sulfate, and water. Subsequently, the absorbing organic carbon (OC) and dust were supplemented to the model by Arola et al. (2011) and Wang et al. (2012), respectively. By joint use of the refractive index, single scattering albedo, sphericity, and other measurements, Van Beelen et al. (2014) and Xie et al. (2017) greatly increased the identifiable aerosol components. Besides, internal mixing and hygroscopic growth of aerosols were also considered in the algorithms to reproduce the real state (Schuster et al., 2016; Zhang et al., 2018a, 2020).

However, the aerosol vertical distribution is not available from the sun-photometer, which can be made up by the ground-based lidar with its vertical resolution of meters. Burton et al. (2012) and Groß et al. (2011) found the characteristics of different aerosol types in lidar parameters, proving the feasibility of lidar. Nishizawa et al. (2007) made use of dual-wavelength elastic lidar but only separated water-soluble aerosol from dust or sea salt. After that, the application of Raman lidar and more wavelengths made it possible to get the profiles of sea salt, soot, dust, and water-soluble

aerosols (Nishizawa et al., 2011, 2017; Hara et al., 2018). Mamouri and Ansmann (2017) refined the fine and coarse dust and separated them from maritime and anthropogenic aerosols based on a polarization/Raman lidar. However, limited by the available lidar information, there has been no breakthrough in the aerosol types identified by lidar measurements. Therefore, how to use limited lidar channels to distinguish more atmospheric aerosol components is what we need to investigate. And considering the advantages and limitations of sun-photometer and lidar, it may be a good choice to combine them.

In this study, based on the synergy of ground-based Mie lidar and sun-photometer in Generalized Aerosol Retrieval from Radiometer and Lidar Combined data (GARRLiC), a new algorithm to get the vertical profiles of fine-mode aerosol components, including BC, water-insoluble organic matter (WIOM), water-soluble organic matter (WSOM), ammonium nitrate-like (AN), and fine aerosol water (AW) content, is proposed for the first time. The details about the algorithm and the measurement data applied to the algorithm will be described in Sect. 2. Section 3 will present the evaluation, uncertainty analysis, and application of our algorithm to confirm the validity of inversion results.

2 Methodology and data

2.1 Methodology

2.1.1 Aerosol microphysical characteristics

Atmospheric aerosol is a complicated mixture of different components, which have different size distributions and complex refractive indexes (CRIs). This makes it possible to separate aerosol components by remote sensing. However, we should note that the aerosol components in the remote-sensing model are not completely equivalent to the chemical compositions traditionally, and there are some limitations in identifying compositions compared with surface chemical measurements. For example, distinguishing sulfate and nitrate seems to be beyond the scope of remote sensing due to their similar optical properties in light scattering, particle size, and shape. Despite all of this, the common remote-sensing components, including black carbon (BC), brown carbon (BrC), dust, organic matter (OM), ammonium nitrate-like (AN), sea salt, and water uptake, are close to the species defined in the Intergovernmental Panel on Climate Change (IPCC) 2013 (Boucher et al., 2013) and enough to satisfy the need for climate change and environmental monitoring. In fact, there are often different aerosol definitions and classification schemes focusing on some key components, which depend on the limited inputs and specific research purposes. Generally, sea-salt aerosol is considered as coarse particles and neglected in Beijing (Li et al., 2013). Dust and OM have similar light-absorbing characteristics due to the pres-

ence of hematite (Formenti et al., 2014). Therefore, they are usually separated by particle size since OM and dust are mostly present in fine- and coarse-mode aerosols, respectively (Schuster et al., 2016; Zhang et al., 2018a). Certainly, fine-mode dust will also be taken into account with sufficient constraints. By assuming the dust volume concentration ratio of fine to coarse mode, Xie et al. (2017) further separated fine- and coarse-mode dust with the aid of spectra refractivity at four wavelengths, sphericity, and single scattering albedos. Besides, they also defined OM as non-absorbing and hydrophobic aerosols to be separated from inorganic salt and absorbing carbon (BC and BrC), while Zhang et al. (2018a) divided the OM into two categories (WIOM and WSOM) to better model complex liquid systems, and BrC is considered as a part of WIOM.

In this paper, considering the limited lidar constraints (only two wavelengths), we only focus on fine-mode aerosol and treat it as a mixture of five components like Zhang et al. (2018a): BC, OM (WIOM + WSOM), AN, and AW, and omit the presence of dust in fine mode to optimize the algorithm performance, although it seems to not cover all possible aerosol types in the atmosphere. Exactly as in Table 1, BC has the largest CRI at different wavelengths, which indicates its strong optical absorption (Mueller et al., 2007; Burton et al., 2012). On the contrary, AN (denoting the inorganic salt such as nitrate and sulfate) is mainly characterized by scattering with the smallest CRI, except for AW (Zhang et al., 2012; Xu and Penner, 2012). Generally, AW content directly depends on the hygroscopic AN at a certain ambient relative humidity (RH), especially in heavy haze episodes (Zhang et al., 2015). With the properties of spectral absorbing, WIOM is significantly different from BC in water-insoluble matter. While in water-soluble ones, hygroscopicity is the key to distinguishing WSOM and AN. According to the summary in Zhang et al. (2018a), the growth factors of inorganic salts are all above 1.5, much larger than that of WSOM. Thus, it is considered that the aerosol hygroscopicity only comes from AN rather than WSOM in this algorithm to separate them.

Based on the distinct aerosol microphysical characteristics, we retrieve the profiles of the fine-mode aerosol components by constructing the aerosol model and microphysical parameterization schemes. Figure 1 shows the flowchart of our algorithm proposed in this study and the details will be described below.

2.1.2 Fine-mode aerosol properties from GARRLiC

In fact, there have been developed algorithms that combine the sun-/sky- photometer with lidar. For pursuing an even deeper synergy of lidar and sun-photometer, GARRLiC was created by modification of AERONET algorithms to adapt them for inclusion of lidar data (Lopatin et al., 2013). As a part of the extensive Generalized Retrieval of Atmosphere and Surface Properties (GRASP), it can get the property profiles separately for fine- and coarse-mode particles. So far,

Table 1. Microphysical parameters of atmospheric aerosol components used in this paper, including CRI, mean radius r_m and geometric standard deviation σ of the lognormal distribution, and density. The relevant literature is given in the last row of the table.

		BC	WIOM	WSOM	AN	AW
CRI	532 nm	$1.95 - 0.79i$	$1.56 - 0.06i$	$1.53 - 0.003i$	$1.41 - 2.3 \times 10^{-3} i$	1.33
	1064 nm	$1.95 - 0.79i$	$1.54 - 0.001i$	$1.53 - 0.001i$	$1.40 - 6.8 \times 10^{-3} i$	1.33
r_m (µm)		0.095	0.126	0.126	0.17	–
σ		1.8	1.49	1.49	2	–
ρ (g cm^{-3})		2.0	1.2	1.2	1.76	1.0
References		Van Beelen et al. (2014), Ganguly et al. (2009), Schuster et al. (2005)	Kirchstetter et al. (2004), Schuster et al. (2016), Ganguly et al. (2009), Dey et al. (2006)	Arola et al. (2011), Ganguly et al. (2009)	Hess et al. (1998), Ganguly et al. (2009), Van Beelen et al. (2014)	Dey et al. (2006), Schuster et al. (2005), Van Beelen et al. (2014)
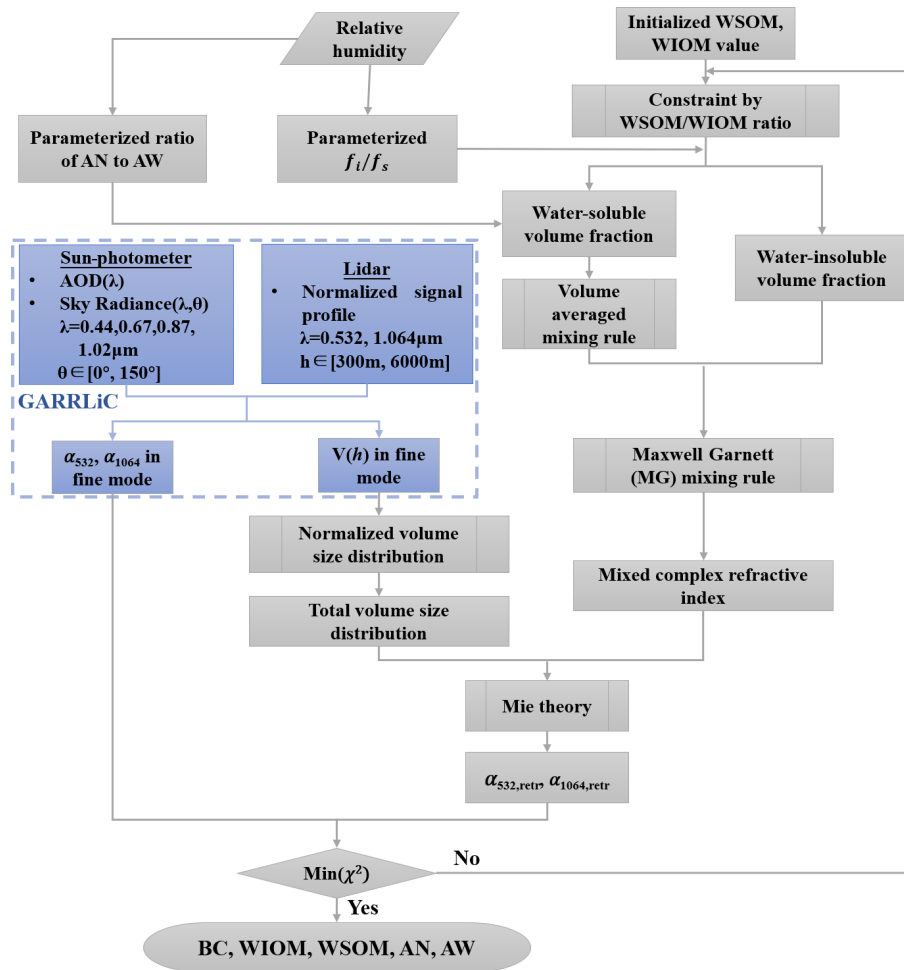
Figure 1. Flowchart of the algorithm proposed in this paper.

GARRLiC has been applied for the characterization of atmospheric aerosols (Lopatin et al., 2013; Tsekeri et al., 2017; Bovchaliuk et al., 2016) and evaluated by airborne in situ measurements (Benavent-Oltra et al., 2021, 2017). Although GARRLiC was able to quantitatively retrieve aerosol components (L. Li et al., 2019), it still stayed on the columnar level and cannot get the flexible volume proportion of different components vertically.

Note particularly that the volume concentration profiles provided by GARRLiC build a bridge between the retrieval of sun-photometer and lidar. In previous lidar algorithms, lidar parameters such as lidar ratio (the ratio of extinction to backscattered coefficients) were employed to avoid the use of volume concentration. But now, due to the accessible volume concentration, complex refractive index (CRI) and volume size distribution (VSD) can be directly used to construct the aerosol model in lidar algorithms based on the Mie theory (Bohren and Huffman, 1998). Consequently, the combination of ground-based remote-sensing technology not only

enriches the inversion output but also provides a new idea for lidar inversion.

However, the Mie theory is only applicable to spherical particles, which is in contradiction with the irregular shape of dust aerosols (Mamouri and Ansmann, 2014; Sugimoto et al., 2002). In retrieval algorithms, it is generally assumed that the aerosol size distribution is bimodal and the dust aerosol is distributed in the coarse mode (Nishizawa et al., 2007, 2011; Schuster et al., 2016; Xie et al., 2017; Zhang et al., 2018a). Therefore, in this study, we only focus on the profiles of fine aerosol components based on the outputs of GARRLiC, which include the aerosol extinction and volume concentration profiles in the fine mode. Similar to AERONET (Dubovik and King, 2000), the radius of 0.576 μm was used as a separation point in GARRLiC. According to the field experiments, the retrieved fine-mode aerosol components, including BC, WIOM, WSOM, and AN, were almost distributed in PM_1 (particles with the aerodynamic diameter less than 1 μm) (Liu et al., 2020; Reddington et al., 2013; Zhang

et al., 2018b). To some extent, the fine modal truncation radius of 0.576 µm is reasonable for inversion.

2.1.3 Aerosol modeling

In the actual atmosphere, the internal mixing of aerosols is very common due to aerosol collision, condensation, and chemical reactions. Generally, the Maxwell Garnett (MG) mixing rule is more appropriate for the mixture of water-insoluble matter embedded in the host environment (Choi and Ghim, 2016; Dey et al., 2006; Schuster et al., 2005). The effective permittivity of the mixture ε_{mix} can be expressed as follows:

$$\varepsilon_{\text{mix}}(\lambda) = \varepsilon_{\text{host}} + 3\varepsilon_{\text{host}} \left[\frac{\sum_j \frac{\varepsilon_j(\lambda) - \varepsilon_{\text{host}}(\lambda)}{\varepsilon_j(\lambda) + 2\varepsilon_{\text{host}}(\lambda)} f_j}{1 - \sum_j \frac{\varepsilon_j(\lambda) - \varepsilon_{\text{host}}(\lambda)}{\varepsilon_j(\lambda) + 2\varepsilon_{\text{host}}(\lambda)} f_j} \right]$$

$$j = \text{BC and WIOM}, \tag{1}$$

where f_j is the volume fraction of water-insoluble components: BC and WIOM. Here, the host environment represents the mixture of water-soluble matter, including AN, WSOM, and AW. The effective permittivities of the host environment and insoluble matter are $\varepsilon_{\text{host}}$ and ε_j, respectively, which can be calculated from the corresponding CRIs by Eq. (2):

$$m = \sqrt{\frac{|\varepsilon(\lambda)| + Re(\varepsilon(\lambda))}{2}} + i\sqrt{\frac{|\varepsilon(\lambda)| - Re(\varepsilon(\lambda))}{2}}, \tag{2}$$

where m and ε are the CRI and effective permittivity, respectively. For the CRI of the host environment m_{host}, which refers to the water-soluble matter, can be obtained by the volume-averaged (VA) mixing rule to strengthen the physical constraints between multi-component liquid systems (Zhang et al., 2018a).

$$m_{\text{host}}(\lambda) = \frac{\sum_j m_j(\lambda) f_j}{\sum_j f_j}$$

$$j = \text{AN, AW, and WSOM}, \tag{3}$$

where m_j and f_j are the CRI and volume fraction of soluble components, respectively. Then the CRI of the aerosol mixture m_{mix} can be acquired by combining Eqs. (1)–(3).

In addition to CRI, VSD is the other requirement for the Mie theory. Here, the normalized VSD of each component can be simulated according to the lognormal distribution parameters in Table 1, which are all in the dry state. Considering the hygroscopicity of AN, the growth factor is introduced to fit the AN normalized VSD under ambient RH (AW is taken into account at the same time). Then, we can model the normalized VSD of the aerosol mixture based on the assumed component volume fraction f_j as follows:

$$\frac{dV_N(\ln r)}{d\ln r} = \sum_{j=1}^{4} f_j \frac{dV_j(\ln r)}{d\ln r}$$

$$j = \text{AN, BC, WIOM, and WSOM}, \tag{4}$$

where $\frac{dV_N(\ln r)}{d\ln r}$ is the normalized VSD of the aerosol mixture and $\frac{dV_j(\ln r)}{d\ln r}$ is the normalized VSD of component j. It can be expressed by Eq. (5):

$$\frac{dV_j(\ln r)}{d\ln r} = \frac{1}{\sqrt{2\pi}|\ln \sigma_j|} \exp\left[-\frac{1}{2}\left(\frac{\ln r - \ln r_j}{\ln \sigma_j}\right)^2 \right], \tag{5}$$

where σ_j and r_j are the geometric standard deviation and mean radius of component j, respectively, which are listed in Table 1.

Combining the fine-mode volume concentration profiles $V(h)$ from GARRLiC, the extinction coefficients at different wavelengths and levels $\sigma_{\text{m}}(\lambda, h)$ can be modeled according to the Mie theory:

$$\sigma_{\text{m}}(\lambda, h) = \int \frac{3}{4r^2} Q_{\text{ext}}(\lambda, r, m) \frac{dV(\ln r)}{d\ln r} d\ln r, \tag{6}$$

where Q_{ext} is the Mie efficiency factor, which is related to lidar wavelength, particle size, and CRI (Bohren and Huffman, 1998); $\frac{dV(\ln r)}{d\ln r}$ can be obtained by $V(h)\frac{dV_N(\ln r)}{d\ln r}$.

Finally, the residual between modeled extinction σ_{m} and fine-mode extinction from GARRLiC σ_{c} is quantified by the iterative kernel function χ^2 to find the optimal combination of component volume fractions:

$$\chi^2 = \sum_\lambda \frac{(\sigma_{\text{m}}(\lambda, h) - \sigma_{\text{c}}(\lambda, h))^2}{\epsilon_{\text{g}}(\lambda, h)(\sigma_{\text{c}}(\lambda, h))^2}$$

$$\lambda = 532, 1064 \text{ nm}, \tag{7}$$

where $\epsilon_{\text{g}}(\lambda, h)$ is the relative fitting residual between lidar measurement and modeled lidar signal from GARRLiC at different wavelengths, which is added to avoid the interference of the uncertainty resulting from GARRLiC modeling. Further, the component volume fractions can be transformed to the mass concentrations $M_j(h)$ by the density (ρ_j) of aerosol component j:

$$M_j(h) = f_j(h) \times V(h) \times \rho_j$$

$$j = \text{AN, AW, BC, WIOM, and WSOM.} \tag{8}$$

2.1.4 Microphysical parameterization scheme

The matched number of input parameters and the output aerosol types is the prerequisite for a reasonable aerosol model. Due to the limitation of lidar wavelengths, the input parameters of lidar are not as many as sun-photometer. Therefore, the aerosol parameterization scheme should be constructed to establish the relationship between aerosol components, thereby reducing the number of unknowns. In our algorithm, we separated water-soluble and water-insoluble aerosols firstly by the parameterization scheme of Zhang et al. (2018a), which was re-parameterized with RH based on Schuster et al. (2009). The volume ratio of water-

insoluble to water-soluble matter can be expressed as follows:

$$\frac{f_i}{f_s} = \varphi(\mathrm{RH}) \int \varepsilon(D)\mathrm{d}D \tag{9}$$

$$\varphi(\mathrm{RH}) = 5.74(1 - \mathrm{RH})^3 + 0.01 \tag{10}$$

$$\varepsilon(D) = \varepsilon_0 + \varepsilon_v \times \exp\left[-\left(\frac{\log(D/d_0)}{\sigma_{\log}}\right)^2\right] \tag{11}$$

where f_i and f_s are the water-insoluble and water-soluble volume fractions respectively. $\varphi(\mathrm{RH})$ is the re-parameterized part of the function with RH. $\varepsilon(D)$ is the climatological function of water-soluble volume fraction and D is the aerosol diameter. ε_0, ε_v, d_0 and $\sigma_{\log}$ are the average fitting parameters in Kandler and Schuetz (2007), which can represent the general aerosol properties. Moreover, $f_i + f_s = 1$ is an important guarantee for the success of retrieval.

For the water-soluble matter, we assumed that AN was the only hygroscopic component as mentioned in Sect. 2.1.1. For enhancing the interaction between AN and AW, the relationship between solute mass concentration and water activity was applied in our algorithm, which was investigated in Tang (1996). And the volume ratio of AN to AW can be obtained by combining the Eqs. (12)–(15):

$$a_w = 1 + \sum_{k=1}^{4} C_k x^k \tag{12}$$

$$\mathrm{RH} = a_w/100 \tag{13}$$

$$\rho_s = 0.9971 + \sum_{k=1}^{4} A_k x^k \tag{14}$$

$$\frac{f_{\mathrm{AN}}}{f_{\mathrm{AN}} + f_{\mathrm{AW}}} = x \frac{\rho(x)}{\rho(100)} \tag{15}$$

where a_w is the water activity, which can be approximately regarded as RH due to the lower curvature effect (Tang, 1996). ρ_s is the density of solution and x is the weight percent of AN. C_k and A_k are the polynomial coefficient of ammonium nitrate from Tang (1996), which is considered as the representative of inorganic salt. f_{AN} and f_{AW} are the volume fractions of AN and AW respectively. With that, the growth factor (GF) of AN can also be acquired, which plays a vital role in the aerosol normalized volume distribution model of Sect. 2.1.3.

$$\mathrm{GF}(\mathrm{RH}) = \frac{r_{\mathrm{wet}}(\mathrm{RH})}{r_{\mathrm{dry}}} = \sqrt[3]{\frac{f_{\mathrm{AN}} + f_{\mathrm{AW}}}{f_{\mathrm{AN}}}} \tag{16}$$

where r_{dry} is the dry particle radius; r_{wet} is the particle radius under the ambient RH.

Fine-mode aerosols are categorized into water-insoluble aerosols and water-soluble aerosols according to the above relationship, which can be quantified with the help of the climatological parameterization scheme in Eq. (9). For water-

insoluble aerosols (BC and WIOM), once the volume fraction of one is known, the volume fraction of other is determined. Meanwhile, for water-soluble aerosols (AN, AW, and WSOM), the relationship between AN and AW is established by Eq. (15), so that AN and AW can be considered as a whole. Thus, only two unknowns, one from water-soluble species and the other from water-insoluble species, are enough to achieve our requirement. In our algorithm, we iteratively changed the volume fractions of WIOM and WSOM and those of AN, AW, and BC can be correspondingly obtained. What's more, we also constrained the relationship between WSOM and WIOM to ensure the reliability of inversion. The ratio of WSOM mass concentration to the total OM is limited to 0.44 to 0.77, which has been applied in Zhang et al. (2018a) according to the statistics of observation experiments.

In summary, as presented in Fig. 1, if the volume fractions of WIOM and WSOM are initialized, the other species would be determined with the aid of parameterization schemes. Then the extinction coefficient can be calculated by the constructed aerosol model. Through multiple iterations and the constraints of fine-mode extinction coefficients from GARRLiC, the optimal combination of volume fractions will be found. Subsequently, the optimal mass concentration results are compared with surface components measurements and model products, including OM, BC, and AN, which verifies the inversion performance of our algorithm. Besides, the possible sources of error are discussed and the uncertainties from these sources are assessed in Sect. 3.2.

2.2 Measurement data

2.2.1 The input data of GARRLiC

The input data of GARRLiC consist of sun-photometer sun and sky radiance, and lidar signals. Here, the sun-photometer measurements were from the Beijing station (39.977° N, 116.381° E) of the AERONET (Aerosol Robotic Network, https://aeronet.gsfc.nasa.gov/, last access: 28 September 2022) in February of 2021. The sky radiance (raw almucantar with 26 scattering angles) and the version 3 level 1.5 product (i.e., automatically cloud cleared but may not have final calibration applied) of total optical depth (TOD) at 440, 675, 870, and 1020 nm were applied to drive GARRLiC. Besides, the AERONET products of fine aerosol optical depth (AOD) and fine volume concentration were employed to validate the outputs from GARRLiC.

For the available sky radiance sequence, the correlative lidar signal data were chosen from a dual-wavelength elastic lidar in the corresponding ±15 min time window, which was set up on the roof of a 28 m high building in the tower of the Institute of Atmospheric Physics at the Chinese Academy of Sciences (39.976° N, 116.378° E). The normalized lidar signals at 532 and 1064 nm were used to run the GARRLiC with the sun-photometer data. In advance, the lidar signals were

averaged for 15 min and computed for 60 log-spaced heights between 150 and 6000 m above the ground to avoid the instrumental error just as the Eq. (17):

$$P'_k = P_k / \int_{Z_{\min}}^{Z_{\max}} P_k \mathrm{d}Z, \qquad (17)$$

where P'_k is the normalized lidar signal and P_k is the raw averaged lidar signal. The upper and lower height limits are represented by $Z_{\max}$ and $Z_{\min}$, respectively. Besides, for the accuracy of GARRLiC, the cases with the relative residual larger than 15 % in the inversion process have been eliminated according to Benavent-Oltra et al. (2021). Consequently, there were 133 retrievals remaining in February of 2021.

2.2.2 Relative humidity data

The vertical profile of relative humidity (RH) data used in our algorithm was interpolated linearly from the European Centre for Medium-Range Weather Forecast (ECMWF) Reanalysis v5 (ERA5) hourly data from 1000 to 300 hPa, which has been verified by the sounding data from the University of Wyoming (http://weather.uwyo.edu/upperair/bufrraob.shtml, last access: 20 September 2022) in Fig. S1 of Supplement.

2.2.3 Components data

The mass concentrations of aerosol components near the surface on 8–15 February 2021, including water-soluble inorganic salt, BC, and OC, were provided by the China National Environmental Monitoring Center to validate the results of the retrieved components. Besides, the Nested Air Quality Prediction Model System (NAQPMS), a three-dimensional chemistry transport model developed by the Institute of Atmospheric Physics (IAP; Li et al., 2012), was also employed to verify the reliability of estimated component profiles. The meteorology field was provided by the Weather Research and Forecasting model (WRF), which is driven by Final Analysis data (FNL) from the National Center for Environmental Prediction (NCEP). The outputs of the NAQPMS used in this paper have been assimilated through the Parallel Data Assimilation Framework (PDAF) system, which has a fairly good correlation with measurements (Wang et al., 2022).

For comparable aerosol components, we used the sum of the water-soluble inorganic salt from surface measurements and NAQPMS products, such as sulfate, nitrate, and ammonium, were used to compare with AN. Due to the limited available data, the mass concentration of OC multiplied by the conversion factor of 1.7 (Bürki et al., 2020) was considered as the observed organics to compare with the total retrieved OM (WIOM + WSOM). The estimated BC can be directly validated by the observation data and model products. In this study, in addition to the correlation coefficient (R), two statistics of root-mean-square error (RMSE) and

normalized mean bias (NMB) were introduced to evaluate the algorithm performance, which can be expressed as follows:

$$\mathrm{RMSE} = \sqrt{\frac{\sum_{i=1}^{n} (X_r - X_o)^2}{n}} \qquad (18)$$

$$\mathrm{NMB} = \frac{\sum_{i=1}^{n} (X_r - X_o)}{\sum_{i=1}^{n} X_o}, \qquad (19)$$

where X_r represents different aerosol components of BC, AN, and OM; n is the sample size; X_o is the corresponding components from surface measurements and NAQPMS products. As an index to measure the deviation from true values (Wang et al., 2021), NMB > 0 indicates the overestimation of estimated results – the larger the value, the greater the overestimation.

## 3 Results and discussion

3.1 Validation

3.1.1 Evaluation of the outputs from GARRLiC

Since GARRLiC provides the input and constraints for our algorithm, whether the GARRLiC outputs are reliable directly determines the accuracy of the component inversion. Therefore, the GARRLiC outputs have to be validated based on the products of AERONET, which are widely used in the validation of remote-sensing results (Che et al., 2009). Due to the unavailable volume concentration profile of AERONET, Fig. 2a presents the comparison of fine columnar volume concentration between GARRLiC and AERONET. It's clear that the correlation coefficient can be up to 0.94 and RMSE was only 0.017. The mean percentage error (MPE), which is the average percent of error from the truth, was about 42 %. This deviation was acceptable since the estimated uncertainty for CRI in the Level 2 AERONET products is about 50 % (Dubovik et al., 2000). Moreover, the extinction coefficients from GARRLiC were also compared with the results retrieved by the Fernald method (Fernald, 1984) with the lidar ratio of 50 sr (Wang et al., 2020). From Fig. 2b we can see that the two results were highly consistent and the correlation coefficient was close to 1. Figure 2c shows the vertical distribution of extinction coefficients from GARRLiC and lidar. Obviously, the extinction average and standard deviation profiles of the two almost coincided, confirming the validity of the GARRLiC outputs. In fact, the extinction profiles from GARRLiC depend directly on the fine-mode AOD and the aerosol vertical profiles (unit: km^{-1}), which are retrieved by lidar signal. Therefore, we validated the fine-mode AOD and fitting lidar signal with AERONET and lidar signal
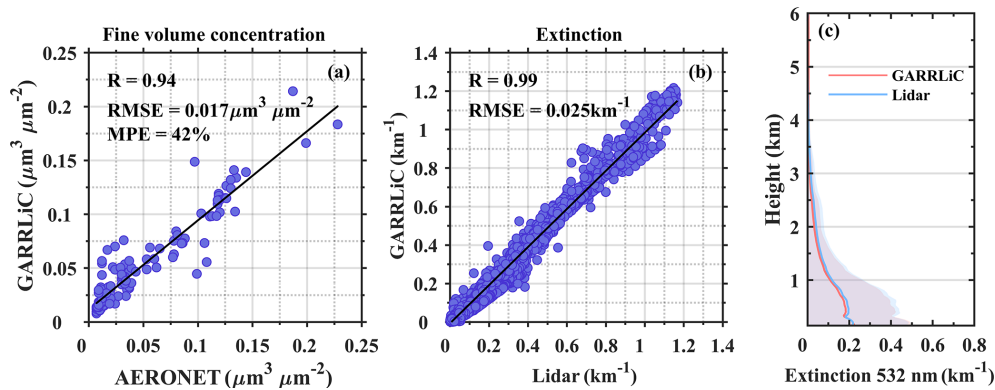
Figure 2. (a) The comparison of fine volume concentration between GARRLiC and AERONET; **(b)** the comparison of extinction coefficient at 532 nm between GARRLiC and lidar; **(c)** the averaged vertical extinction profiles from GARRLiC and lidar in February of 2021. The shadows with different colors represent the standard deviation of extinction profiles from GARRLiC and lidar.
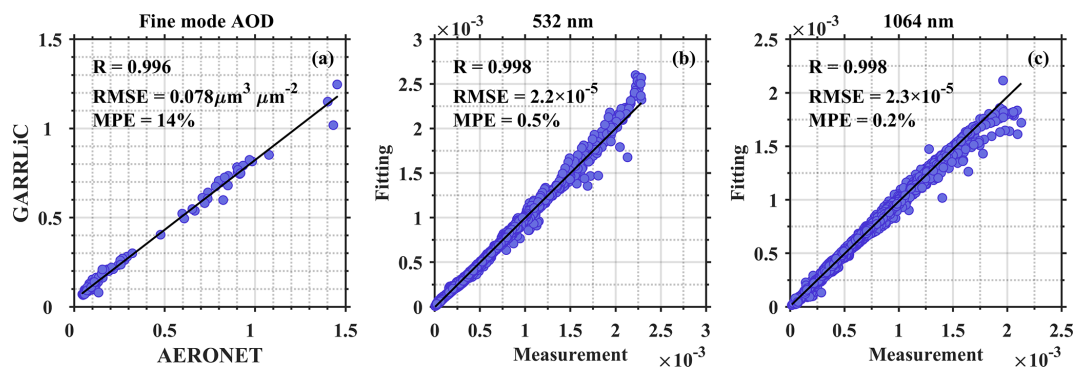
Figure 3. (a) The comparison of fine-mode AOD between GARRLiC and AERONET; the comparison of lidar signal between the fit from GARRLiC and measurement at **(b)** 532 nm and **(c)** 1064 nm.

measurements, respectively. As shown in Fig. 3, not only the fine-mode AOD but also the fitting lidar signal was in good agreement with their respective reference, with the correlation coefficient greater than 0.99. And the total MPEs of fine extinction at two wavelengths were both about 14 %, largely dependent on the fine-mode AOD due to the little error in vertical lidar signal fitting. All of the above analyses indicate that the fine volume concentration and extinction profiles from GARRLiC are reliable enough to drive the component retrieval.

3.1.2 Comparison with surface observations

In order to validate the estimated mass concentration of components, the comparison with observations on 8–15 February 2021 is presented here. During the test experiment period, the number of samples was limited by the availability of AERONET data. As shown in Fig. 4a, the fine volume concentration between GARRLiC and AERONET matched well, with a correlation coefficient of 0.89. The NMB of 0.031 indicated the credible results from GARRLiC; but there was still a slight overestimation at high aerosol load-

ing. On 11–12 February 2021, the RH dropped from the peak value companied with decreased extinction coefficients (Fig. 4b–c), and the RH in the experiment period changed from 20 % to 70 %, which was enough to reflect the general atmospheric situation.

Due to the lack of observed component profile, the observed mass concentrations of water-soluble inorganic salt, BC, and OC near the surface were used to verify the remotely sensed results preliminarily. The estimated components from remote sensing at 150 m were employed for the verification. Figure 5 gives the comparable results of AN, BC, and OM between observation and retrieval results at the available time. An encouraging coherence in the variation trend of AN between estimation and observation ($R = 0.67$) was found although there was an underestimation on 12 February. Besides, there was a better consistency between the estimated and observed BC. The correlation coefficient can be up to 0.91. However, the overestimation of BC was obvious on 12 February, which was just the opposite of AN. This deviation can be attributed to the decreasing RH from 11 to 12 February, which influences the parameterization schemes as mentioned in Sect. 2.1.4. Moreover, when the extinction
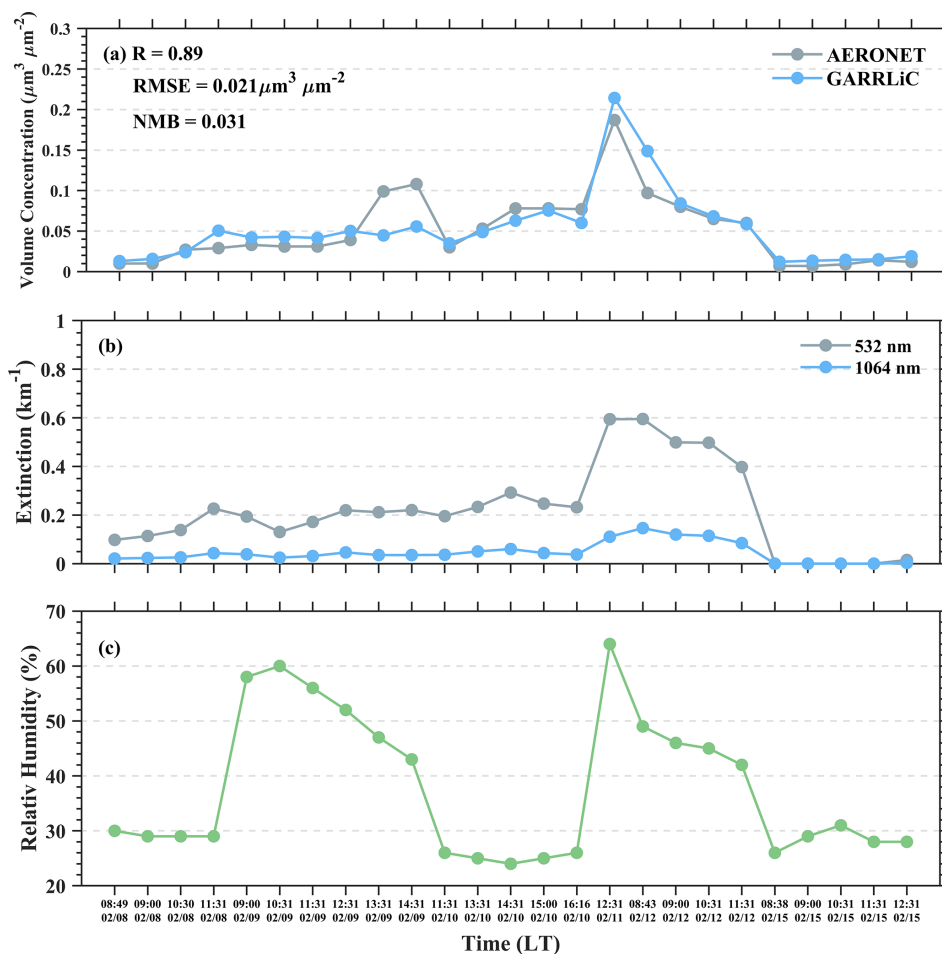
Figure 4. (a) The fine volume concentration from GARRLiC and AERONET; **(b)** the fine-mode extinction at 532 and 1064 nm; **(c)** the RH from ERA5 at the available time on 8–15 February 2021.

coefficients changed little (Fig. 4b), the decreased fine volume concentrations after 12 February also had responsibility for the error, which led to the underestimated total mass concentration relative to observation. As shown in Fig. 5c, the overestimation of OM was evident, and the mass concentrations of WSOM were closer to the observation. We should note that the components in the remote-sensing models are not equivalent to the concepts in chemical research (Z. Li et al., 2019), which is the primary error of comparisons. On the other hand, there must be differences in the mass concentration of aerosol between the surface and 150 m due to the influence of the atmospheric mixing state and emission sources of different aerosol components.

3.1.3 Verification of estimated vertical profiles

Similar to the comparisons with surface observations, the mass concentration of OC multiplied by 1.7 was chosen to compare with OM, and the sum of the nitrate, sulfate, and ammonium salt was used to compare with AN. The estimated AN from remote sensing had the best correlation with

that from NAQPMS ($R = 0.85$ in Table 2), and there was a slight underestimation (NMB $= -0.19$). The BC and OM correlations were relatively weaker, with a correlation coefficient of ~ 0.5, which corresponded to the relationship of OM in Zhang et al. (2018a). The deviation can be explained by the different input RH data of our algorithm and NAQPMS. Moreover, the differences in the results from two different principles are reasonable. After all, our classification of aerosol components is based on their optical characteristics. Here, in order to evaluate the performance of vertical profiles, we present two cases with lower and higher aerosol loading in Fig. 6. It can be seen that the mass concentration profiles of aerosol components from remote sensing and NAQPMS were comparable. In the relatively clean condition, OM had a higher mass concentration than AN, and the vertical distribution of the estimated OM was similar to that from NAQPMS, with the smallest deviation. There were fluctuations in both estimated and simulated AN profiles < 1 km. Subsequently, the maximum local concentration of the estimated AN occurred at 2.5 km, while for simulated AN pro-
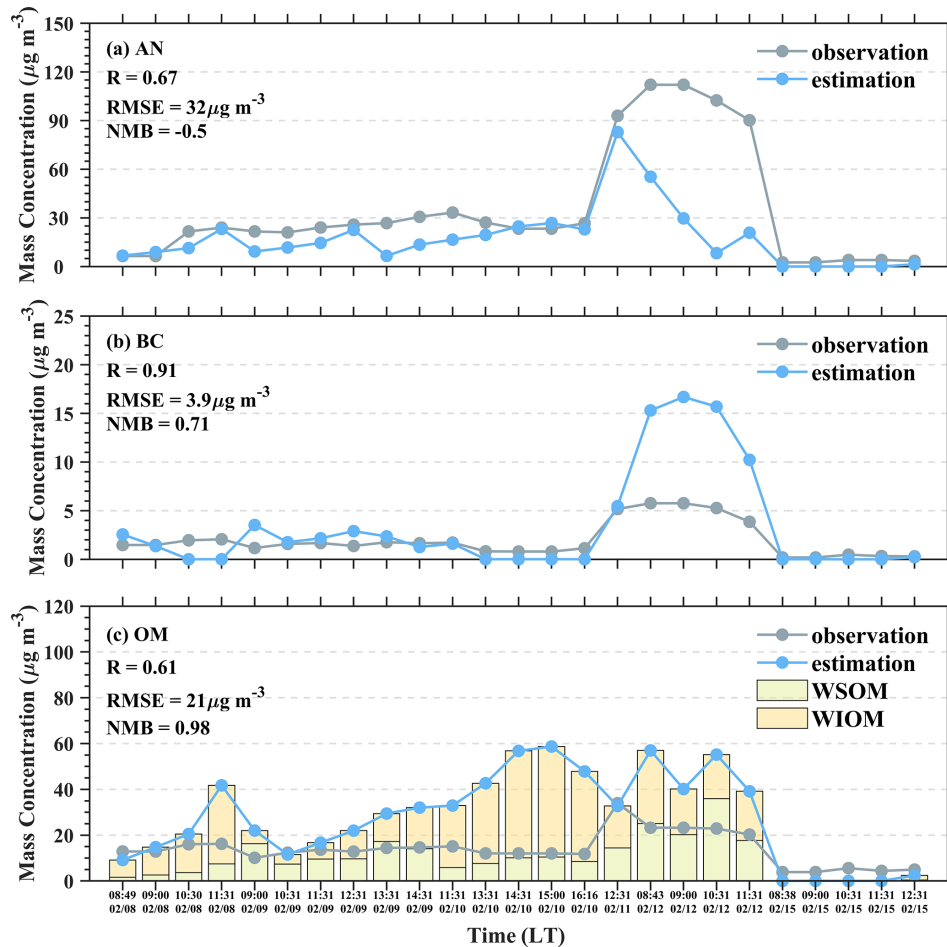
Figure 5. The comparisons between observation and estimation results from remote sensing of **(a)** AN; **(b)** BC; **(c)** OM at available time on 8–15 February 2021.

files, it occurred at ~ 2 km. The two BC profiles had similar distributions. In the case of a higher aerosol load (Fig. 6d–f), AN estimation performed best according to the simulated AN profile from NAQPMS, but still with a little underestimation. In comparison, the overestimation of OM and BC at ~ 1 km was obvious. It is noteworthy that the vertical distribution of different aerosol components was synchronous in both remote sensing and NAQPMS. Therefore, the vertical patterns of components depend largely on that of total extinction profiles, which is why the two results from remote sensing and NAQPMS cannot match exactly.

3.2 Uncertainty assessment of component estimation

In fact, the uncertainties of component retrieval mainly come from the errors of input parameters, i.e., RH, volume concentration, and extinction coefficients. Among them, RH influences the component estimation indirectly by the parameterization schemes, which are closely related to RH. Zhang et al. (2018a) discussed the uncertainty of $\frac{f_i}{f_s}$ caused by φ (RH) and the mean error is about 31.6 % when the RH is no more

Table 2. The correlation coefficient (R), the root mean square error (RMSE), and the normalized mean bias (NMB) of AN, BC, and OM between remote sensing and NAQPMS are presented.

	R	RMSE (μg m^{-3})	NMB
AN	0.85	14.4	−0.19
BC	0.54	5.2	−0.18
OM	0.50	15.9	0.78

than 85 %. Since the influence of RH on a parameterization scheme always exists, here, we take 55 % as the critical point of higher and lower RH to evaluate the uncertainty from input microphysical parameters. In this paper, the Monte Carlo method was employed based on the random generation of input parameters by a Gaussian distribution with the original values and errors as mean and standard deviation, respectively. The error of RH was considered as about 10 % according to the uncertainty from ERA5 (Gamage et al., 2020).
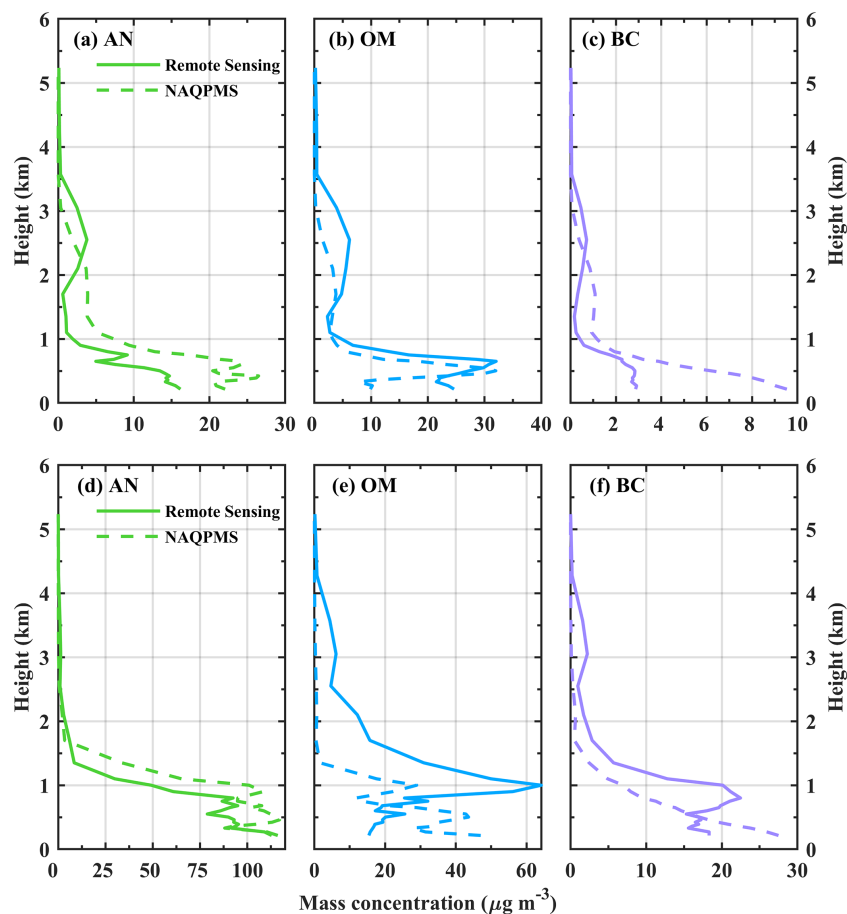
Figure 6. The averaged mass concentration profiles of **(a)** AN; **(b)** OM; **(c)** BC from 11:00 to 13:00 LT on 9 February, 2021; **(d–f)** same as **(a)–(c)** but averaged from 09:00 to 12:00 LT on 11 February, 2021. The solid lines and dashed lines represent the results from remote sensing and NAQPMS, respectively.

Additionally, MPEs of the fine volume concentration and extinction coefficient mentioned in Sect. 3.1.1 were applied in the Monte Carlo method. Each input parameter was sampled with 30 iterations at different heights (Mattis et al., 2016). Relative uncertainty was characterized by the ratio of standard deviation to mean values of 30 iteration results.

The uncertainties of AN, AW, WSOM, BC, and WIOM from RH are given in Fig. 7a, with the mean values of 34.5 %, 48 %, 16.5 %, 40 %, and 7 % under the low-RH condition, and 24.7 %, 40 %, 57 %, 68.8 %, and 65.8 % under the high-RH condition, respectively. For other parameters, there were similar quantitative relationships of the component estimation uncertainties. The uncertainties of AN and AW at higher RH were smaller than those at lower RH for all parameters. That is because the parameterization scheme described in Sect. 2.1.4 is closer to the actual condition at higher RH (Tang, 1996). On the contrary, the higher RH made the larger uncertainties for WIOM, BC, and WSOM, which may be due to the increasing error of $\frac{f_i}{f_s}$ caused by φ (RH) below the RH of 85 % (Zhang et al., 2018a). As shown in Fig. 7b, the larger error of fine volume concentration with 42 % brought

greater uncertainty to component estimation. Similarly, with the input CRI varying by more than 1 order of magnitude, Schuster et al. (2016) found that the uncertainty of BrC can change from 50 % to 440 %. Obviously, the estimation of BC was more sensitive to the input parameters. This may be attributed to the smaller amount of BC, the volume fraction of which is 1–2 orders of magnitude less than that of other components. The uncertainties caused by the constraints of the extinction coefficients were mainly below 50 % for different components, which is comparable with the uncertainty of retrievals by remote sensing (Li et al., 2013). It should be noted that the uncertainty of aerosol components, such as BC in emission inventories, can be 200 % and more (Schuster et al., 2005). Therefore, it is valuable to retrieve by our algorithm.

In fact, some errors exist exactly but are difficult to quantify realistically. Just as the assumption of internal mixing does not apply to all situations, so do the microphysical parameters. Cheng et al. (2012) observed that the number fraction of internally mixed soot in total soot particles had pronounced diurnal cycles. When the aging process converts
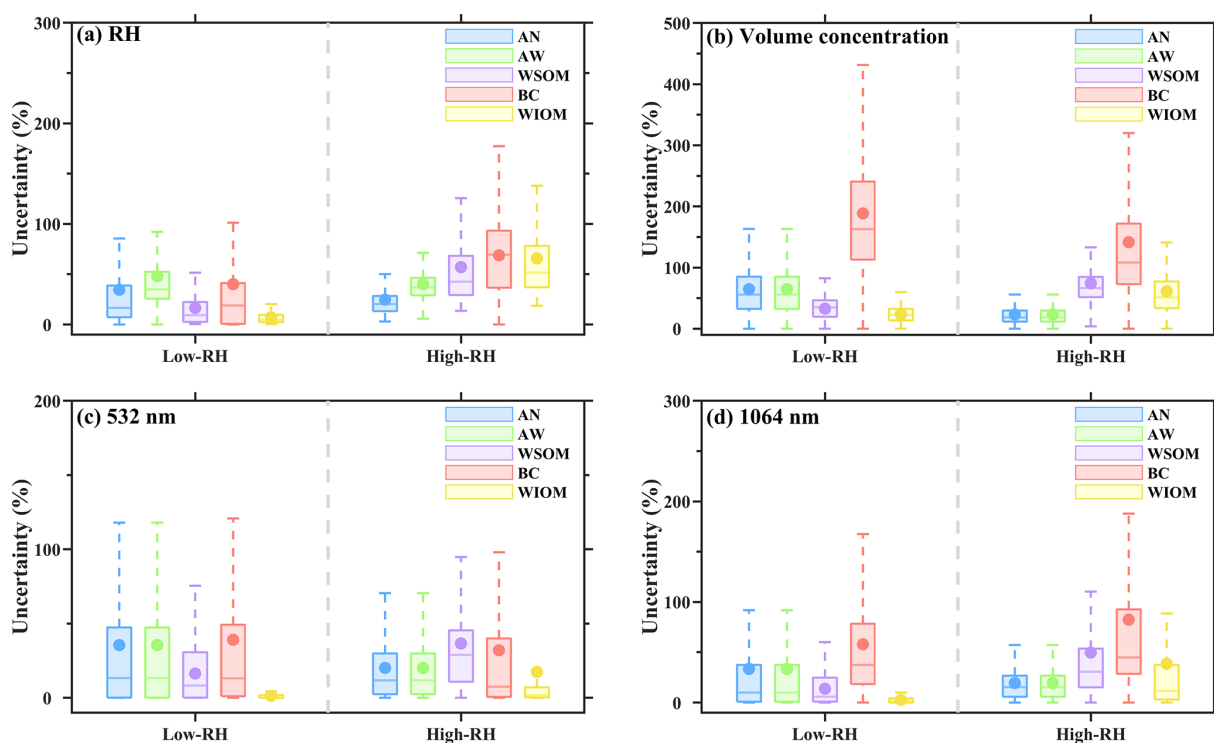
Figure 7. The uncertainty of component retrieval from **(a)** RH with the error of 10 %; **(b)** volume concentration with the error of 42 %; extinction coefficient with the error of 14 % at **(c)** 532 nm; **(d)** 1064 nm.

externally mixed soot into internally mixed ones, emissions tend to emit more fresh and externally mixed soot particles. Another unquantifiable error is from the Mie theory based on the spherical hypothesis, which idealizes aerosol particles. However, the uncertainties related to assumptions are endemic to all retrievals by remote sensing, as well as the chemistry transport models (Chen et al., 2019). We should mention that field measurement also cannot avoid inconsistent assumptions.

3.3 The application of retrieval algorithm

3.3.1 Optical closure test

Based on the measurement data of lidar and sun-photometer in February of 2021, the mass concentration profiles of aerosol components in Beijing were retrieved. Figure 8 shows a quantitative optical closure test under different RH conditions to validate the consistency between recovered extinction and the constraints from GARRLiC. It can be seen that the modeled extinctions at 532 and 1064 nm both had a good correlation with the reference values. The correlation coefficients were both close to 1. However, there were still some large residuals at the two wavelengths, especially at the RH between 70 %–80 %. It seems to underestimate the extinction when the RH was larger than 70 %. That is probably because the water-insoluble fraction is limited at high RH, and BC in water-insoluble matter tends to contribute greatly

to extinction. On the contrary, the overestimation of 532 nm at the RH of about 30 % can be attributed to the larger proportion of water-insoluble matter. We should realize that the parameterization scheme of water-soluble and water-insoluble matter may have trouble in reflecting the real atmosphere situation. But for now, there are still not sufficient observation experiments to construct a more realistic scheme. Moreover, the added constraint of the relationship between WIOM and WSOM can also limit the BC fraction, although ignoring the constraint could bring about a well-matched closure result but might lead to unreasonable component volume fractions.

3.3.2 Vertical profiles of aerosol components in Beijing

Figure 9 shows two typical cases under different situations. It can be seen that the vertical distribution of aerosol components can be quantified even with extremely low aerosol loading (Fig. 9a). Under the clean condition, aerosols were mainly distributed below 3 km with different patterns of component profiles. There were similar peak values in the mass concentrations of AN and WIOM but at different heights. The mass concentration of AW was the smallest throughout the vertical direction due to the low RH. As shown in Fig. 9b, the two local maximums of RH being about 40 % appeared at about 700 m and 2.4 km, respectively, which was consistent with extinction profiles below 3 km. Besides, there was a fairly good relationship between the optical fit extinc-
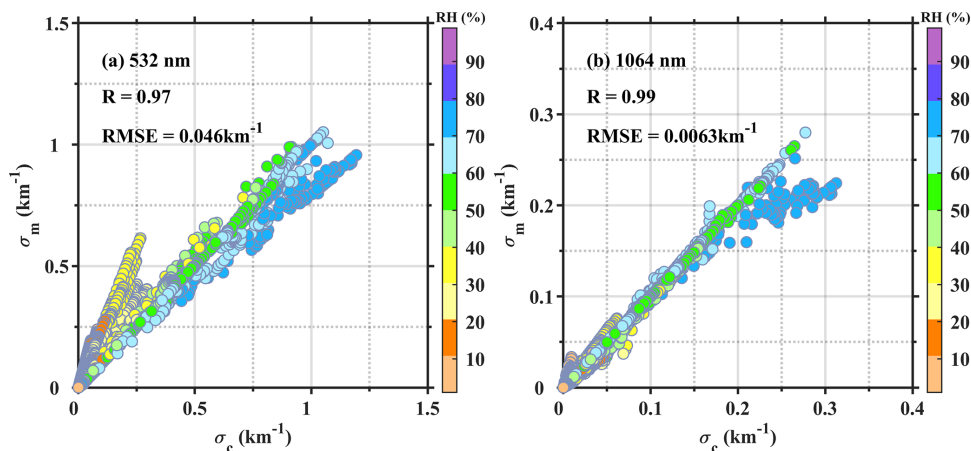
Figure 8. The comparison between modeled extinction σ_m and extinction constraints from GARRLiC σ_c at (a) 532 nm and (b) 1064 nm.
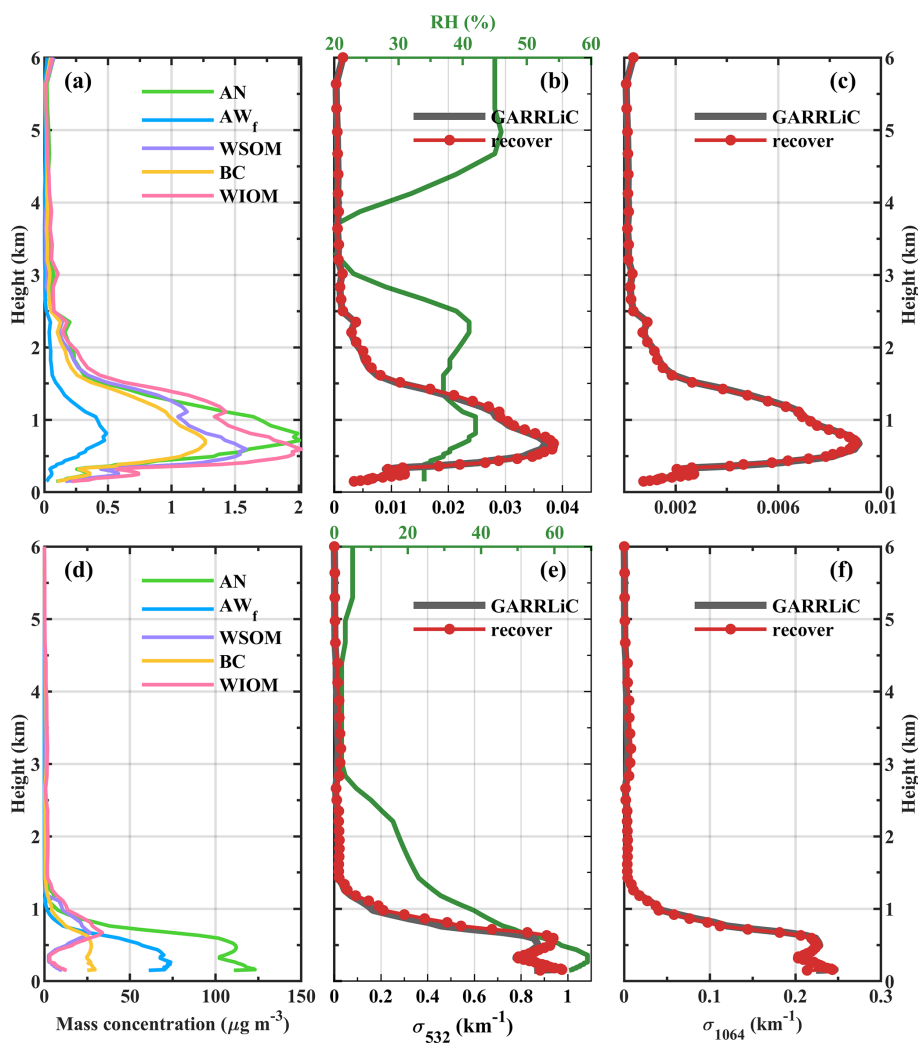
Figure 9. (a) The mass concentration profiles of aerosol components retrieved from remote sensing at 09:00 LT on 7 February 2021, which was under clean conditions; (b) the vertical distribution of relative humidity (RH) (green line) and extinction coefficients at 532 nm at 09:00 LT on 7 February 2021. The dotted red line represents the extinction profile recovered by the component results and the dark gray line represents the input data from GARRLiC; (c) the vertical distribution of extinction coefficients at 1064 nm at 09:00 LT on 7 February 2021; (d–f) same as (a)–(c) but for 12:29 LT on 26 February 2021, which was under polluted conditions.

tions and inputs from GARRLiC with a mean relative error of 4.63 % at 532 nm and -1.99 % at 1064 nm (Fig. 9c).

In the polluted case, aerosol components were concentrated below 1 km due to the weak atmospheric diffusion capacity as shown in Fig. 9d. The maximum mass concentration of AN occurred near the surface, being about $125\,\mu g\,m^{-3}$. Subsequently, there was a decreasing trend with a fluctuation between about 300 to 600 m, while the mass concentration of WIOM and WSOM peaked at 672 m and were only about $10\,\mu g\,m^{-3}$ near the ground. According to Lou et al. (2017), sulfate and nitrate, transformed from SO_2 and NO_2, were mainly responsible for the fine particle pollution at the RH of about 70 %, which explains the high proportion of AN in Fig. 9d. Generally, pollution is usually accompanied by high RH. As shown in Fig. 9e, the maximum RH matched the large value of extinction below 1 km well. Moreover, the well-recovered extinction profiles at two lidar wavelengths indicated the stability of our algorithm.

4 Conclusions

By combining ground-based lidar and sun-photometer, we develop a new algorithm to get the vertical profiles of fine-mode aerosol components, including black carbon (BC), water-insoluble organic matter (WIOM), water-soluble organic matter (WSOM), ammonium nitrate-like (AN), and fine aerosol water (AW) content, which increases the retrieved aerosol types from the dual-wavelength Mie lidar. On this basis, the vertical profiles of aerosol components obtained in February 2021 in Beijing are retrieved and compared with in situ measurements and simulated results from NAQPMS, proving the validity of our component estimation. There is the best consistency between the estimated and observed BC with a correlation coefficient up to 0.91. The trend of AN between estimation and observation is accordant but with a little underestimation. Meanwhile, compared with the simulated results, the retrieved AN from remote sensing had the best correlation ($R = 0.85$) with a slight underestimation (NMB $= -0.19$). The BC and OM correlations were relatively weaker, with a correlation coefficient of ~ 0.5. The vertical distribution of different aerosol components was synchronous in both remote sensing and NAQPMS. Considering the distinct principles, the differences between remote sensing and simulated results are reasonable to some extent. In addition, the reliability of the retrieval algorithm is also verified by the well-recovered extinction coefficients in the quantitative optical closure test.

Based on the products of AERONET, the mean errors obtained with respect to the input parameters are introduced to assess the uncertainty of component estimation by the Monte Carlo method. The uncertainties caused by extinction coefficients are mainly less than 50 % for different components. Additionally, increasingly better component estimation results can be obtained with the increasing accuracy of the input parameters. However, errors from the assumptions, such as internal mixing and spherical hypothesis, are difficult to quantify realistically. Further, we should mention that the assumptions are endemic to all retrievals by remote sensing. Meanwhile, the parameterization schemes and aerosol microphysical parameters used in the algorithm, which vary over time and place, still need to be improved by conducting sufficient observation experiments. In the future, the distinguishable aerosol types will be increased by upgrading parameterization schemes, employing more lidar wavelengths, and considering the irregular shape of dust.

References

Andrews, T. and Forster, P. M.: Energy budget constraints on historical radiative forcing, Nat. Clim. Chang., 10, 313–316, https://doi.org/10.1038/s41558-020-0696-1, 2020.

Arola, A., Schuster, G., Myhre, G., Kazadzis, S., Dey, S., and Tripathi, S. N.: Inferring absorbing organic carbon content from AERONET data, Atmos. Chem. Phys., 11, 215–225, https://doi.org/10.5194/acp-11-215-2011, 2011.

Benavent-Oltra, J. A., Román, R., Granados-Muñoz, M. J., Pérez-Ramírez, D., Ortiz-Amezcua, P., Denjean, C., Lopatin, A., Lyamani, H., Torres, B., Guerrero-Rascado, J. L., Fuertes, D., Dubovik, O., Chaikovsky, A., Olmo, F. J., Mallet, M., and Alados-Arboledas, L.: Comparative assessment of GRASP algorithm for a dust event over Granada (Spain) during ChArMEx-ADRIMED 2013 campaign, Atmos. Meas. Tech., 10, 4439–4457, https://doi.org/10.5194/amt-10-4439-2017, 2017.

Benavent-Oltra, J. A., Casquero-Vera, J. A., Román, R., Lyamani, H., Pérez-Ramírez, D., Granados-Muñoz, M. J., Herrera, M., Cazorla, A., Titos, G., Ortiz-Amezcua, P., Bedoya-Velásquez, A. E., de Arruda Moreira, G., Pérez, N., Alastuey, A., Dubovik, O., Guerrero-Rascado, J. L., Olmo-Reyes, F. J., and Alados-Arboledas, L.: Overview of the SLOPE I and II campaigns: aerosol properties retrieved with lidar and sun–sky photometer measurements, Atmos. Chem. Phys., 21, 9269–9287, https://doi.org/10.5194/acp-21-9269-2021, 2021.

Bian, H. S., Prather, M. J., and Takemura, T.: Tropospheric aerosol impacts on trace gas budgets through photolysis, J. Geophys. Res.-Atmos., 108, 4242, https://doi.org/10.1029/2002jd002743, 2003.

Bohren, C. F. and Huffman, D. R.: Absorption and Scattering by a Sphere, in: Absorption and Scattering of Light by Small Particles, Wiley, 82–129, https://doi.org/10.1002/9783527618156.ch4, 1998.

Boucher, O., Randall, D., Artaxo, P., Bretherton, C., Feingold, G., Forster, P., Kerminen, V.-M., Kondo, Y., Liao, H., and Lohmann, U.: Clouds and aerosols, in: Climate change 2013: the physical science basis. Contribution of Working Group I to the Fifth Assessment Report of the Intergovernmental Panel on Climate Change, Cambridge University Press, 571–657, https://doi.org/10.1017/CBO9781107415324.016, 2013.

Bovchaliuk, V., Goloub, P., Podvin, T., Veselovskii, I., Tanre, D., Chaikovsky, A., Dubovik, O., Mortier, A., Lopatin, A., Korenskiy, M., and Victori, S.: Comparison of aerosol properties retrieved using GARRLiC, LIRIC, and Raman algorithms applied to multi-wavelength lidar and sun/sky-photometer data, Atmos. Meas. Tech., 9, 3391–3405, https://doi.org/10.5194/amt-9-3391-2016, 2016.

Bürki, C., Reggente, M., Dillner, A. M., Hand, J. L., Shaw, S. L., and Takahama, S.: Analysis of functional groups in atmospheric aerosols by infrared spectroscopy: method development for probabilistic modeling of organic carbon and organic matter concentrations, Atmos. Meas. Tech., 13, 1517–1538, https://doi.org/10.5194/amt-13-1517-2020, 2020.

Burton, S. P., Ferrare, R. A., Hostetler, C. A., Hair, J. W., Rogers, R. R., Obland, M. D., Butler, C. F., Cook, A. L., Harper, D. B., and Froyd, K. D.: Aerosol classification using airborne High Spectral Resolution Lidar measurements – methodology and examples, Atmos. Meas. Tech., 5, 73–98, https://doi.org/10.5194/amt-5-73-2012, 2012.

Che, H., Zhang, X., Chen, H., Damiri, B., Goloub, P., Li, Z., Zhang, X., Wei, Y., Zhou, H., Dong, F., Li, D., and Zhou, T.: Instrument calibration and aerosol optical depth validation of the China Aerosol Remote Sensing Network, J. Geophys. Res.-Atmos., 114, D03206, https://doi.org/10.1029/2008jd011030, 2009.

Chen, C., Dubovik, O., Henze, D. K., Chin, M., Lapyonok, T., Schuster, G. L., Ducos, F., Fuertes, D., Litvinov, P., Li, L., Lopatin, A., Hu, Q., and Torres, B.: Constraining global aerosol emissions using POLDER/PARASOL satellite remote sensing observations, Atmos. Chem. Phys., 19, 14585–14606, https://doi.org/10.5194/acp-19-14585-2019, 2019.

Chen, Y., Zhao, C., Zhang, Q., Deng, Z., Huang, M., and Ma, X.: Aircraft study of Mountain Chimney Effect of Beijing, China, J. Geophys. Res.-Atmos., 114, D08306, https://doi.org/10.1029/2008jd010610, 2009.

Cheng, Y. F., Su, H., Rose, D., Gunthe, S. S., Berghof, M., Wehner, B., Achtert, P., Nowak, A., Takegawa, N., Kondo, Y., Shiraiwa, M., Gong, Y. G., Shao, M., Hu, M., Zhu, T., Zhang, Y. H., Carmichael, G. R., Wiedensohler, A., Andreae, M. O., and Pöschl, U.: Size-resolved measurement of the mixing state of soot in the megacity Beijing, China: diurnal cycle, aging and parameterization, Atmos. Chem. Phys., 12, 4477–4491, https://doi.org/10.5194/acp-12-4477-2012, 2012.

Chew, B. N., Campbell, J. R., Salinas, S. V., Chang, C. W., Reid, J. S., Welton, E. J., Holben, B. N., and Liew, S. C.: Aerosol particle vertical distributions and optical properties over Singapore, Atmos. Environ., 79, 599–613, https://doi.org/10.1016/j.atmosenv.2013.06.026, 2013.

Choi, Y. and Ghim, Y. S.: Estimation of columnar concentrations of absorbing and scattering fine mode aerosol components using AERONET data, J. Geophys. Res.-Atmos., 121, 13628–13640, https://doi.org/10.1002/2016jd025080, 2016.

Dey, S., Tripathi, S. N., Singh, R. P., and Holben, B. N.: Retrieval of black carbon and specific absorption over Kanpur city, northern India during 2001-2003 using AERONET data, Atmos. Environ., 40, 445–456, https://doi.org/10.1016/j.atmosenv.2005.09.053, 2006.

Dubovik, O. and King, M. D.: A flexible inversion algorithm for retrieval of aerosol optical properties from Sun and sky radiance measurements, J. Geophys. Res.-Atmos., 105, 20673–20696, https://doi.org/10.1029/2000JD900282, 2000.

Dubovik, O., Smirnov, A., Holben, B. N., King, M. D., Kaufman, Y. J., Eck, T. F., and Slutsker, I.: Accuracy assessments of aerosol optical properties retrieved from Aerosol Robotic Network (AERONET) Sun and sky radiance measurements, J. Geophys. Res.-Atmos., 105, 9791–9806, https://doi.org/10.1029/2000jd900040, 2000.

Dubovik, O., Holben, B., Eck, T. F., Smirnov, A., Kaufman, Y. J., King, M. D., Tanre, D., and Slutsker, I.: Variability of absorption and optical properties of key aerosol types observed in worldwide locations, J. Atmos. Sci., 59, 590–608, https://doi.org/10.1175/1520-0469(2002)059<0590:Voaaop>2.0.Co;2, 2002.

Fernald, F. G.: Analysis of atmospheric lidar observations: some comments, Appl. Opt., 23, 652–653, https://doi.org/10.1364/ao.23.000652, 1984.

Formenti, P., Caquineau, S., Chevaillier, S., Klaver, A., Desboeufs, K., Rajot, J. L., Belin, S., and Briois, V.: Dominance of goethite over hematite in iron oxides of mineral dust from Western Africa: Quantitative partitioning by X-ray absorption spectroscopy, J. Geophys. Res.-Atmos., 119, 12740–12754, https://doi.org/10.1002/2014JD021668, 2014.

Gamage, S. M., Sica, R. J., Martucci, G., and Haefele, A.: A 1D Var Retrieval of Relative Humidity Using the ERA5 Dataset for the Assimilation of Raman Lidar Measurements, J. Atmos. Ocean. Tech., 37, 2051–2064, https://doi.org/10.1175/jtech-d-19-0170.1, 2020.

Ganguly, D., Ginoux, P., Ramaswamy, V., Dubovik, O., Welton, J., Reid, E. A., and Holben, B. N.: Inferring the composition and concentration of aerosols by combining AERONET and MPLNET data: Comparison with other measurements and utilization to evaluate GCM output, J. Geophys. Res.-Atmos., 114, D16203, https://doi.org/10.1029/2009jd011895, 2009.

Groß, S., Tesche, M., Freudenthaler, V., Toledano, C., Wiegner, M., Ansmann, A., Althausen, D., and Seefeldner, M.: Characterization of Saharan dust, marine aerosols and mixtures of biomass-burning aerosols and dust by means of multi-wavelength depolarization and Raman lidar measurements during SAMUM 2, Tellus B, 63, 706–724, https://doi.org/10.1111/j.1600-0889.2011.00556.x, 2011.

Gu, Y., Liou, K. N., Xue, Y., Mechoso, C. R., Li, W., and Luo, Y.: Climatic effects of different aerosol types in China simulated by the UCLA general circulation model, J. Geophys. Res.-Atmos., 111, D15201, https://doi.org/10.1029/2005jd006312, 2006.

Han, T., Xu, W., Chen, C., Liu, X., Wang, Q., Li, J., Zhao, X., Du, W., Wang, Z., and Sun, Y.: Chemical apportionment of aerosol optical properties during the Asia-Pacific Economic Cooperation summit in Beijing, China, J. Geophys. Res.-Atmos., 120, 12281–12295, https://doi.org/10.1002/2015jd023918, 2015.

Hara, Y., Nishizawa, T., Sugimoto, N., Osada, K., Yumimoto, K., Uno, I., Kudo, R., and Ishimoto, H.: Retrieval of Aerosol Components Using Multi-Wavelength Mie-Raman Lidar and Comparison with Ground Aerosol Sampling, Remote Sens., 10, 937, https://doi.org/10.3390/rs10060937, 2018.

Hasekamp, O. P., Gryspeerdt, E., and Quaas, J.: Analysis of polarimetric satellite measurements suggests stronger cooling due to aerosol-cloud interactions, Nat. Commun., 10, 5405, https://doi.org/10.1038/s41467-019-13372-2, 2019.

Hess, M., Koepke, P., and Schult, I.: Optical properties of aerosols and clouds: The software package OPAC, B. Am. Meteorol. Soc., 79, 831–844, https://doi.org/10.1175/1520-0477(1998)079<0831:Opoaac>2.0.Co;2, 1998.

Huang, J., Hsu, N. C., Tsay, S.-C., Jeong, M.-J., Holben, B. N., Berkoff, T. A., and Welton, E. J.: Susceptibility of aerosol optical thickness retrievals to thin cirrus contamination during the BASE-ASIA campaign, J. Geophys. Res.-Atmos., 116, D08214, https://doi.org/10.1029/2010jd014910, 2011.

Huang, R.-J., Zhang, Y., Bozzetti, C., Ho, K.-F., Cao, J.-J., Han, Y., Daellenbach, K. R., Slowik, J. G., Platt, S. M., Canonaco, F., Zotter, P., Wolf, R., Pieber, S. M., Bruns, E. A., Crippa, M., Ciarelli, G., Piazzalunga, A., Schwikowski, M., Abbaszade, G., Schnelle-Kreis, J., Zimmermann, R., An, Z., Szidat, S., Baltensperger, U.,

El Haddad, I., and Prevot, A. S. H.: High secondary aerosol contribution to particulate pollution during haze events in China, Nature, 514, 218–222, https://doi.org/10.1038/nature13774, 2014.

Jiang, Y., Liu, X., Yang, X.-Q., and Wang, M.: A numerical study of the effect of different aerosol types on East Asian summer clouds and precipitation, Atmos. Environ., 70, 51–63, https://doi.org/10.1016/j.atmosenv.2012.12.039, 2013.

Kandler, K. and Schuetz, L.: Climatology of the average water-soluble volume fraction of atmospheric aerosol, Atmos. Res., 83, 77–92, https://doi.org/10.1016/j.atmosres.2006.03.004, 2007.

Kirchstetter, T. W., Novakov, T., and Hobbs, P. V.: Evidence that the spectral dependence of light absorption by aerosols is affected by organic carbon, J. Geophys. Res.-Atmos., 109, D21208, https://doi.org/10.1029/2004jd004999, 2004.

Li, J., Wang, Z., Wang, X., Yamaji, K., Takigawa, M., Kanaya, Y., Pochanart, P., Liu, Y., Irie, H., Hu, B., Tanimoto, H., and Akimoto, H.: Impacts of aerosols on summertime tropospheric photolysis frequencies and photochemistry over Central Eastern China, Atmos. Environ., 45, 1817–1829, https://doi.org/10.1016/j.atmosenv.2011.01.016, 2011.

Li, J., Wang, Z., Zhuang, G., Luo, G., Sun, Y., and Wang, Q.: Mixing of Asian mineral dust with anthropogenic pollutants over East Asia: a model case study of a super-duststorm in March 2010, Atmos. Chem. Phys., 12, 7591–7607, https://doi.org/10.5194/acp-12-7591-2012, 2012.

Li, J., Fu, Q., Huo, J., Wang, D., Yang, W., Bian, Q., Duan, Y., Zhang, Y., Pan, J., Lin, Y., Huang, K., Bai, Z., Wang, S.-H., Fu, J. S., and Louie, P. K. K.: Tethered balloon-based black carbon profiles within the lower troposphere of Shanghai in the 2013 East China smog, Atmos. Environ., 123, 327–338, https://doi.org/10.1016/j.atmosenv.2015.08.096, 2015.

Li, L., Dubovik, O., Derimian, Y., Schuster, G. L., Lapyonok, T., Litvinov, P., Ducos, F., Fuertes, D., Chen, C., Li, Z., Lopatin, A., Torres, B., and Che, H.: Retrieval of aerosol components directly from satellite and ground-based measurements, Atmos. Chem. Phys., 19, 13409–13443, https://doi.org/10.5194/acp-19-13409-2019, 2019.

Li, Z., Gu, X., Wang, L., Li, D., Xie, Y., Li, K., Dubovik, O., Schuster, G., Goloub, P., Zhang, Y., Li, L., Ma, Y., and Xu, H.: Aerosol physical and chemical properties retrieved from ground-based remote sensing measurements during heavy haze days in Beijing winter, Atmos. Chem. Phys., 13, 10171–10183, https://doi.org/10.5194/acp-13-10171-2013, 2013.

Li, Z., Xie, Y., Zhang, Y., Li, L., Xu, H., Li, K., and Li, D.: Advance in the remote sensing of atmospheric aerosol composition, J. Remote Sens., 23, 359–373, 2019.

Liao, H., Yung, Y. L., and Seinfeld, J. H.: Effects of aerosols on tropospheric photolysis rates in clear and cloudy atmospheres, J. Geophys. Res.-Atmos., 104, 23697–23707, https://doi.org/10.1029/1999jd900409, 1999.

Liu, H., Pan, X., Wu, Y., Ji, D., Tian, Y., Chen, X., and Wang, Z.: Size-resolved mixing state and optical properties of black carbon at an urban site in Beijing, Sci. Total Environ., 749, 141523, https://doi.org/10.1016/j.scitotenv.2020.141523, 2020.

Lopatin, A., Dubovik, O., Chaikovsky, A., Goloub, P., Lapyonok, T., Tanré, D., and Litvinov, P.: Enhancement of aerosol characterization using synergy of lidar and sun-photometer coincident observations: the GARRLiC algorithm, Atmos. Meas. Tech., 6, 2065–2088, https://doi.org/10.5194/amt-6-2065-2013, 2013.

Lou, C. R., Liu, H. Y., Li, Y. F., Peng, Y., Wang, J., and Dai, L. J.: Relationships of relative humidity with PM$_{2.5}$ and PM$_{10}$ in the Yangtze River Delta, China, Environ. Monit. Assess., 189, 582, https://doi.org/10.1007/s10661-017-6281-z, 2017.

Lou, S., Liao, H., and Zhu, B.: Impacts of aerosols on surface-layer ozone concentrations in China through heterogeneous reactions and changes in photolysis rates, Atmos. Environ., 85, 123–138, https://doi.org/10.1016/j.atmosenv.2013.12.004, 2014.

Mamouri, R. E. and Ansmann, A.: Fine and coarse dust separation with polarization lidar, Atmos. Meas. Tech., 7, 3717–3735, https://doi.org/10.5194/amt-7-3717-2014, 2014.

Mamouri, R.-E. and Ansmann, A.: Potential of polarization/Raman lidar to separate fine dust, coarse dust, maritime, and anthropogenic aerosol profiles, Atmos. Meas. Tech., 10, 3403–3427, https://doi.org/10.5194/amt-10-3403-2017, 2017.

Mattis, I., D'Amico, G., Baars, H., Amodeo, A., Madonna, F., and Iarlori, M.: EARLINET Single Calculus Chain – technical – Part 2: Calculation of optical products, Atmos. Meas. Tech., 9, 3009–3029, https://doi.org/10.5194/amt-9-3009-2016, 2016.

Mueller, D., Ansmann, A., Mattis, I., Tesche, M., Wandinger, U., Althausen, D., and Pisani, G.: Aerosol-type-dependent lidar ratios observed with Raman lidar, J. Geophys. Res.-Atmos., 112, D16202, https://doi.org/10.1029/2006jd008292, 2007.

Myhre, G., Samset, B. H., Schulz, M., Balkanski, Y., Bauer, S., Berntsen, T. K., Bian, H., Bellouin, N., Chin, M., Diehl, T., Easter, R. C., Feichter, J., Ghan, S. J., Hauglustaine, D., Iversen, T., Kinne, S., Kirkevåg, A., Lamarque, J.-F., Lin, G., Liu, X., Lund, M. T., Luo, G., Ma, X., van Noije, T., Penner, J. E., Rasch, P. J., Ruiz, A., Seland, Ø., Skeie, R. B., Stier, P., Takemura, T., Tsigaridis, K., Wang, P., Wang, Z., Xu, L., Yu, H., Yu, F., Yoon, J.-H., Zhang, K., Zhang, H., and Zhou, C.: Radiative forcing of the direct aerosol effect from AeroCom Phase II simulations, Atmos. Chem. Phys., 13, 1853–1877, https://doi.org/10.5194/acp-13-1853-2013, 2013.

Nishizawa, T., Okamoto, H., Sugimoto, N., Matsui, I., Shimizu, A., and Aoki, K.: An algorithm that retrieves aerosol properties from dual-wavelength polarized lidar measurements, J. Geophys. Res.-Atmos., 112, D06212, https://doi.org/10.1029/2006jd007435, 2007.

Nishizawa, T., Sugimoto, N., Matsui, I., Shimizu, A., and Okamoto, H.: Algorithms to retrieve optical properties of three component aerosols from two-wavelength backscatter and one-wavelength polarization lidar measurements considering non-sphericity of dust, J. Quant. Spectrosc. Ra., 112, 254–267, https://doi.org/10.1016/j.jqsrt.2010.06.002, 2011.

Nishizawa, T., Sugimoto, N., Matsui, I., Shimizu, A., Hara, Y., Itsushi, U., Yasunaga, K., Kudo, R., and Kim, S. W.: Ground-based network observation using Mie-Raman lidars and multi-wavelength Raman lidars and algorithm to retrieve distributions of aerosol components, J. Quant. Spectrosc. Ra., 188, 79–93, https://doi.org/10.1016/j.jqsrt.2016.06.031, 2017.

Ran, L., Deng, Z., Xu, X., Yan, P., Lin, W., Wang, Y., Tian, P., Wang, P., Pan, W., and Lu, D.: Vertical profiles of black carbon measured by a micro-aethalometer in summer in the North China Plain, Atmos. Chem. Phys., 16, 10441–10454, https://doi.org/10.5194/acp-16-10441-2016, 2016.

Reddington, C. L., McMeeking, G., Mann, G. W., Coe, H., Frontoso, M. G., Liu, D., Flynn, M., Spracklen, D. V., and Carslaw, K. S.: The mass and number size distributions of black carbon aerosol over Europe, Atmos. Chem. Phys., 13, 4917–4939, https://doi.org/10.5194/acp-13-4917-2013, 2013.

Schuster, G. L., Dubovik, O., Holben, B. N., and Clothiaux, E. E.: Inferring black carbon content and specific absorption from Aerosol Robotic Network (AERONET) aerosol retrievals, J. Geophys. Res.-Atmos., 110, D10S17, https://doi.org/10.1029/2004jd004548, 2005.

Schuster, G. L., Lin, B., and Dubovik, O.: Remote sensing of aerosol water uptake, Geophys. Res. Lett., 36, L03814, https://doi.org/10.1029/2008gl036576, 2009.

Schuster, G. L., Dubovik, O., and Arola, A.: Remote sensing of soot carbon – Part 1: Distinguishing different absorbing aerosol species, Atmos. Chem. Phys., 16, 1565–1585, https://doi.org/10.5194/acp-16-1565-2016, 2016.

Shimizu, A., Nishizawa, T., Jin, Y., Kim, S. W., Wang, Z. F., Batdorj, D., and Sugimoto, N.: Evolution of a lidar network for tropospheric aerosol detection in East Asia, Opt. Eng., 56, 031219, https://doi.org/10.1117/1.Oe.56.3.031219, 2017.

Sugimoto, N., Matsui, I., Shimizu, A., Uno, I., Asai, K., Endoh, T., and Nakajima, T.: Observation of dust and anthropogenic aerosol plumes in the Northwest Pacific with a two-wavelength polarization lidar on board the research vessel Mirai, Geophys. Res. Lett., 29, 1901, https://doi.org/10.1029/2002GL015112, 2002.

Tang, I. N.: Chemical and size effects of hygroscopic aerosols on light scattering coefficients, J. Geophys. Res.-Atmos., 101, 19245–19250, https://doi.org/10.1029/96jd03003, 1996.

Tsekeri, A., Lopatin, A., Amiridis, V., Marinou, E., Igloffstein, J., Siomos, N., Solomos, S., Kokkalis, P., Engelmann, R., Baars, H., Gratsea, M., Raptis, P. I., Binietoglou, I., Mihalopoulos, N., Kalivitis, N., Kouvarakis, G., Bartsotas, N., Kallos, G., Basart, S., Schuettemeyer, D., Wandinger, U., Ansmann, A., Chaikovsky, A. P., and Dubovik, O.: GARRLiC and LIRIC: strengths and limitations for the characterization of dust and marine particles along with their mixtures, Atmos. Meas. Tech., 10, 4995–5016, https://doi.org/10.5194/amt-10-4995-2017, 2017.

van Beelen, A. J., Roelofs, G. J. H., Hasekamp, O. P., Henzing, J. S., and Röckmann, T.: Estimation of aerosol water and chemical composition from AERONET Sun–sky radiometer measurements at Cabauw, the Netherlands, Atmos. Chem. Phys., 14, 5969–5987, https://doi.org/10.5194/acp-14-5969-2014, 2014.

Wang, F., Yang, T., Wang, Z., Chen, X., Wang, H., and Guo, J.: A comprehensive evaluation of planetary boundary layer height retrieval techniques using lidar data under different pollution scenarios, Atmos. Res., 253, 105483, https://doi.org/10.1016/j.atmosres.2021.105483, 2021.

Wang, H., Yang, T., and Wang, Z.: Development of a coupled aerosol lidar data quality assurance and control scheme with Monte Carlo analysis and bilateral filtering, Sci. Total Environ., 728, 138844, https://doi.org/10.1016/j.scitotenv.2020.138844, 2020.

Wang, H., Yang, T., Wang, Z., Li, J., Chai, W., Tang, G., Kong, L., and Chen, X.: An aerosol vertical data assimilation system (NAQPMS-PDAF v1.0): development and application, Geosci. Model Dev., 15, 3555–3585, https://doi.org/10.5194/gmd-15-3555-2022, 2022.

Wang, L., Li, Z.-Q., Li, D.-H., Li, K.-T., Tian, Q.-J., Li, L., Zhang, Y., Lu, Y., and Gu, X.-F.: Retrieval of Dust Fraction of Atmospheric Aerosols Based on Spectra Characteristics of Refractive Indices Obtained from Remote Sensing

Measurements, Spectrosc. Spect. Anal., 32, 1644–1649, https://doi.org/10.3964/j.issn.1000-0593(2012)06-1644-06, 2012.

Xia, X. G.: A critical assessment of direct radiative effects of different aerosol types on surface global radiation and its components, J. Quant. Spectrosc. Ra., 149, 72–80, https://doi.org/10.1016/j.jqsrt.2014.07.020, 2014.

Xie, Y. S., Li, Z. Q., Zhang, Y. X., Zhang, Y., Li, D. H., Li, K. T., Xu, H., Zhang, Y., Wang, Y. Q., Chen, X. F., Schauer, J. J., and Bergin, M.: Estimation of atmospheric aerosol composition from ground-based remote sensing measurements of Sun-sky radiometer, J. Geophys. Res.-Atmos., 122, 498–518, https://doi.org/10.1002/2016jd025839, 2017.

Xing, J., Wang, J., Mathur, R., Wang, S., Sarwar, G., Pleim, J., Hogrefe, C., Zhang, Y., Jiang, J., Wong, D. C., and Hao, J.: Impacts of aerosol direct effects on tropospheric ozone through changes in atmospheric dynamics and photolysis rates, Atmos. Chem. Phys., 17, 9869–9883, https://doi.org/10.5194/acp-17-9869-2017, 2017.

Xu, L. and Penner, J. E.: Global simulations of nitrate and ammonium aerosols and their radiative effects, Atmos. Chem. Phys., 12, 9479–9504, https://doi.org/10.5194/acp-12-9479-2012, 2012.

Zhang, H., Shen, Z., Wei, X., Zhang, M., and Li, Z.: Comparison of optical properties of nitrate and sulfate aerosol and the direct radiative forcing due to nitrate in China, Atmos. Res., 113, 113–125, https://doi.org/10.1016/j.atmosres.2012.04.020, 2012.

Zhang, Q., Ma, X., Tie, X., Huang, M., and Zhao, C.: Vertical distributions of aerosols under different weather conditions: Analysis of in-situ aircraft measurements in Beijing, China, Atmos. Environ., 43, 5526–5535, https://doi.org/10.1016/j.atmosenv.2009.05.037, 2009.

Zhang, Y., Li, Z., Cuesta, J., Li, D., Wei, P., Xie, Y., and Li, L.: Aerosol Column Size Distribution and Water Uptake Observed during a Major Haze Outbreak over Beijing on January 2013, Aerosol Air Qual. Res., 15, 945–957, https://doi.org/10.4209/aaqr.2014.05.0099, 2015.

Zhang, Y., Li, Z., Sun, Y., Lv, Y., and Xie, Y.: Estimation of atmospheric columnar organic matter (OM) mass concentration from remote sensing measurements of aerosol spectral refractive, Atmos. Environ., 179, 107–117, https://doi.org/10.1016/j.atmosenv.2018.02.010, 2018a.

Zhang, Y., Su, H., Ma, N., Li, G., Kecorius, S., Wang, Z., Hu, M., Zhu, T., He, K., Wiedensohler, A., Zhang, Q., and Cheng, Y.: Sizing of Ambient Particles From a Single-Particle Soot Photometer Measurement to Retrieve Mixing State of Black Carbon at a Regional Site of the North China Plain, J. Geophys. Res.-Atmos., 123, 12778–12795, https://doi.org/10.1029/2018jd028810, 2018b.

Zhang, Y., Li, Z., Chen, Y., de Leeuw, G., Zhang, C., Xie, Y., and Li, K.: Improved inversion of aerosol components in the atmospheric column from remote sensing data, Atmos. Chem. Phys., 20, 12795–12811, https://doi.org/10.5194/acp-20-12795-2020, 2020.

Zhao, X. J., Zhao, P. S., Xu, J., Meng,, W., Pu, W. W., Dong, F., He, D., and Shi, Q. F.: Analysis of a winter regional haze event and its formation mechanism in the North China Plain, Atmos. Chem. Phys., 13, 5685–5696, https://doi.org/10.5194/acp-13-5685-2013, 2013.